Development of constitutive creep damage-based modified Robinson–Rousselier (MRR) model with XFEM for void-crack relation in ductile materials

M.I.M. Ahmad[1] [ID] **· M. Akbar[2] · N.A. Abdullah[3]**

Abstract

In this work, we present the predictive modeling for ductile creep damage by implementing the modified Robinson–Rousselier constitutive relations and extended finite element method (XFEM) to treat creep rupture in the void-crack growth problem. We develop an attractive new model, called the modified Robinson–Rousselier (MRR) model, to predict the creep damage behavior in terms of micromechanical damage due to void growth in the ductile materials. The MRR model interface executes an implicit integration scheme in the UMAT subroutine of the Abaqus/Standard module. The radial return method is performed to integrate the viscoplastic constitutive equation in finite element formulation. The numerical models in 2D and 3D elements are implemented to identify the developed subroutines' correctness, and the results are compared with the exact solution for verification. Furthermore, the tensile creep tests on the smooth bars specimen are modeled and tested at a constant temperature of 625 °C with different stress levels. The results show that the maximum values of stress, creep strain, and void damage are detected near the tensile specimen center, where the necking process is formed. Furthermore, the results are compared with the literature to verify and evaluate the developed model and show a reasonable agreement between both results. Then this analysis is extended by introducing crack development in the specimen based on the XFEM technique. As a result, a new model, called the modified Robinson–Rousselier XFEM (MRRX) model is proposed, and the results are compared with the results found in the literature, which showed the evolutions of void growth in the crack path. Therefore the MRRX model solution is proven to have the potential to predict the creep damage behavior in terms of the void-crack growth in the ductile material structures.

Keywords Creep damage · MRR model · UMAT subroutine · MRRX model · Void-crack growth

✉ M.I.M. Ahmad
  meoriqram@ukm.edu.my

1 Department of Mechanical and Manufacturing Engineering, Faculty of Engineering and Built Environment, Universiti Kebangsaan Malaysia, 43600 UKM Bangi, Selangor, Malaysia

2 Faculty of Mechanical and Aerospace Engineering, Institut Teknologi Bandung, Jalan Ganesha 10, Bandung, Indonesia

3 Department of Mechanical Engineering, Kulliyyah of Engineering, International Islamic University Malaysia, Jalan Gombak, 53100, Malaysia

1 Introduction

In recent years, much effort has been devoted to the development of design criteria for structural components operating under extreme mechanical, thermal, and environmental loading conditions. Structural components, for example, in a nuclear power plant, piping, automotive and aerospace applications, are exposed to the component material failure due to creep damage during operation. Creep failure is the progressive time-dependent and permanently deform of metals under load and elevated temperature conditions, and the rate of creep determines the service life of given materials in engineering. Cavity growth mechanisms have been used to model the damage resulting from the deformation of creep. The nucleation and growth process of cavities varies under different applied loadings and temperatures. The voids normally nucleate around second-phase particles and within the grains in cold forming processes of metals.

Numerous works have been carried out previously that dealt with predictive modeling of creep damage. For example, Becker et al. (2002) presented the damage behavior of uniaxial, biaxial, triaxial, and multimaterial creep using a finite element formulation within continuum damage mechanics (CDM) approach. Followed by Hyde et al. (2006), who performed a finite element analysis on P91[1] pipes under creep damage conditions, an Abaqus user subroutine was incorporated with the modified Kachanov–Rabotnov creep constitutive damage equation to predict the damage and service life of 10CrMo910 heat-resistant steel (Geng et al. 2009). Elsewhere, Roy et al. (2015) proposed a probabilistic model based on discontinuous Markov process where the damage parameter of creep cavitation/voids has been introduced for creep damage assessment.

In the early 1990s, the Robinson creep model was introduced, which represents the creep damage theory for metallic composites with strong fibers. The creep rupture model has been established as an extension of continuum damage mechanics and included an isochronous damage function, which depends on the invariants specifying the local maximum transverse tension and maximum longitudinal shear stress. The first application was made to a thin-wall pressure vessel, and it was reported that the model has a potential as a means of optimizing designs of composite structures where creep and creep rupture are life-limiting (Robinson et al. 1992). After that, NASA Lewis Research Center and Pratt and Whitney Aircraft carried out a test based on the model for estimating the failure pressure of SiC/ Ti test ring subjected to a monotonically increasing pressure at 427 °C (Robinson and Pastor 1992). The Robinson model has become a suitable benchmark for assessing the applicability accuracy of structural analysis and failure prediction methods for metallic composites. Some modification has been made in the model to enhance the solution method such as extension formulation with Bodner's model, representing material anisotropy under hydrostatic stress (Robinson et al. 2003) and with Norton model for predicting creep deformation in transversely isotropy materials (Robinson and Binienda 2001).

To complete the calculations used to estimate the creep deformation and failure life of load-bearing components, it is necessary to have constitutive equations that relate creep strain rates to the potential function and the void damage state of the material. Thus, based on the CDM approach to developing the solution model for a prediction on ductile fracture, Rousselier (2001) proposed an application of linear stability analysis of a perturbation to porous metal plasticity and thermoplasticity. Rousselier et al. (1988) explained in more detail the Rousselier model methodology for ductile fracture analysis based on a local ap-

---

[1]P91 is a type of alloy steel widely used in power and chemical plant applications

proach of fracture and damage mechanics. They proved that this model has the potential to characterize several structural sheets of steel and attempted to predict the effects of inclusion content and temperature as well as crack initiation and growth. Azinpour et al. (2021) proposed several extensions of the Rousselier model for using the phase-field diffusive crack approach by predicting the crack evolution in materials containing voids. The Rousselier model was calibrated against the ductile fracture behavior to predict ductile crack extension under a combination of primary and residual weld stress in the bending test (Arun et al. 2017).

The existence of crack growth in materials promotes a primary mode of material failure. Questions on how crack growth affects the strength of the material structure need to be answered. Much research efforts need to be dedicated to developing appropriate crack growth studies of specific materials either by experimental work or mathematical representation model. For example, the fracture mechanisms based on the crack in the aluminum sheet for the gas-forming process were investigated using an experimental and FE simulation, and the results were successfully compared between both approaches (Gohari et al. 2013). The extended finite element method (XFEM) was used as an effective model to provide advantages in crack growth study for crack modeling (Sanchez-Rivadeneira et al. 2020). This technique is implemented with the discontinuous Heaviside step function. The two-dimensional linear elastic asymptotic crack-tip displacement fields are used to account for the crack. This enables the domain to be modeled by finite elements without explicitly meshing the crack surfaces (Dimitri et al. 2021). This method is often chosen in the study of determining the ductile fracture crack and also for the creep crack growth development. For example, the XFEM solution was performed with Liu–Murakami damage model, which was capable of evaluating the creep cracking propagation for various materials at different temperatures (Pandey et al. 2019).

As a matter of fact, the connection between the Rousselier model and XFEM is fascinating to explore, which can give a new contribution to a knowledge of ductile fracture mechanics, especially for predicting the material behavior of the ductile materials in terms of void-crack growth relation (Sprave and Menzel 2020). It has been proven by Ahmad et al. (2019), who proposed a new model called the RuX model, which is capable to predict the voids damage and cracks extension in the ductile materials. Further investigation has been carried out to analyze the void-crack growth in three-dimensional purpose, where the aluminium wingbox aircraft structure was modeled to pursue the structural integrity assessment based on the RuX model (Ahmad et al. 2018).

Furthermore, it is a good opportunity to take this advantage in solving the material structure problems in creep failure behavior. Until now, there are no published findings that promote the numerical solution of the void-crack growth relation in the creep damage problem. Therefore this work presents a valuable contribution to engineering practice, especially for ductile creep damage mechanics analysis, where the modified Robinson–Rousselier (MRR) model is introduced to represent the creep damage behavior in void growth form. The analysis is extended for solving the crack development in the material where the XFEM is used to account for the crack existence, in which a new model called the modified Robinson–Rousselier XFEM MRRX model has been proposed to complete the investigation of void-crack growth mechanism in creep damage analysis. To the authors' knowledge, this is the first contribution in ductile failure analysis where the micromechanical damage of void-crack relation is used to represent the damage in the constitutive of creep modeling solution, which can give some advantages for the development of engineering knowledge.

2 General framework

2.1 Robinson creep model

In 1992, Robinson and Binienda (2001), Robinson et al. (2003), Haque and Steward (2019) proposed the following viscoelasticity model for creep behavior:

$$\dot{\epsilon}_{ij}^T = \dot{\epsilon}_{ij}^e + \dot{\epsilon}_{ij}^c, \tag{1}$$

where $\dot{\epsilon}_{ij}^T$ denotes the total of strain rate, and $\dot{\epsilon}_{ij}^e$ and $\dot{\epsilon}_{ij}^c$ are the elastic and creep deformation rates. The creep strain rate is given as

$$\dot{\epsilon}_{ij}^c = \frac{3}{2}\dot{\varepsilon}_o \left(\frac{\phi}{\sigma_o}\right)^{n-1} \Gamma_{ij}, \tag{2}$$

$$\Gamma_{ij} = \frac{\partial \phi}{\partial \sigma_{ij}} \tag{3}$$

where Γ_{ij} is the flow rule, ϕ is the dissipation potential function, σ_o is a reference stress, $\dot{\varepsilon}_o$ and n are the material parameters, and σ_{ij} are the components of stress.

2.2 Rousselier's damage model

To estimate the onset of yielding of the material point (Ganjiani 2018; Boyina et al. 2017; Jin and Arson 2018), which shows the presence of the void volume fraction damage, the Rousselier model is used to consider as an internal state variable in the material constitutive model. Areias et al. (2013), Seidenfuss et al. (2011) proposed the classical plastic potential

$$\phi = \frac{\sigma_{eq}}{\rho} - R\left(\varepsilon_{eq}\right) + B\left(\beta\right) D e^{\left(\frac{\sigma_m}{\rho \sigma_1}\right)}, \tag{4}$$

where σ_{eq} and σ_m are the von Mises equivalent and mean stresses, respectively, D and σ_1 are Rousselier material parameters, ρ is the relative density, β is the internal variable describing damage, and ε_{eq} is the equivalent plastic strain, which represents hardening of the material.

By substituting $\rho = 1 - f$ and $B(\beta) = \sigma_1 f$ into Eq. (4) the Rousselier plastic potential can be written as

$$\phi = \frac{\sigma_{eq}}{1 - f} - R\left(\varepsilon_{eq}\right) + D\sigma_1 f e^{\left(\frac{\sigma_m}{(1-f)\sigma_1}\right)}, \tag{5}$$

where f is the void volume fraction damage.

The void growth can be obtained as

$$f_{n+1} = f_n + \Delta f_n, \tag{6}$$

$$\Delta f_{n+1} = \Delta f_n + \frac{(1 - f_n)\Delta \epsilon_v - \Delta f_n}{1 + \Delta \epsilon_v}, \tag{7}$$

where Δf is the void volume fraction increment, $\Delta \epsilon_v$ is the volumetric creep strain increment, and n is the number of iteration.

2.3 Modified Robinson–Rousselier creep damage model

Firstly, the dissipation potential function ϕ in the Robinson model needs to be replaced with the potential function, which represents the behavior of ductile materials. In the modified Robinson–Rousselier (MRR) model equation, the parameter ϕ in the Robinson model is substituted with the dissipation potential function of the Rousselier damage model to acquire the correlation between both models. The general form of the parameter ϕ is given by

$$\phi = \frac{\sigma_{eq}}{1-f} - R\left(\varepsilon_{eq}\right) + D\sigma_1 f e^{\left(\frac{\sigma_m}{(1-f)\sigma_1}\right)}, \tag{8}$$

where D and σ_1 are the material properties of the Rousselier model.

The associated flow rule Γ_{ij} is derived according to volumetric and deviatoric parts as

$$\Gamma_{ij} = \frac{\partial \phi}{\partial \sigma_{ij}} = \left(\frac{\partial \phi}{\partial \tilde{p}}\frac{\partial \tilde{p}}{\partial \sigma_{ij}}\right)_V + \left(\frac{\partial \phi}{\partial \tilde{q}}\frac{\partial \tilde{q}}{\partial \sigma_{ij}}\right)_D \tag{9}$$

$$= \frac{1}{3}d\epsilon_{\tilde{p}}\delta_{ij} + d\epsilon_{\tilde{q}}n_{ij}, \tag{10}$$

where $d\epsilon_{\tilde{p}}$ and $d\epsilon_{\tilde{q}}$ are the variables corresponding to the volumetric and deviatoric creep strain increments.

By substituting Eqs. (8) and (9) into Eq. (2) the creep strain rate for the modified Robinson–Rousselier model equation is defined as

$$\dot{\epsilon}^c_{ij} = \frac{3}{2}\dot{\varepsilon}_o\left[\frac{1}{\sigma_o}\left(\frac{\sigma_{eq}}{1-f} - R\left(\varepsilon_{eq}\right) + D\sigma_1 f e^{\left(\frac{\sigma_m}{(1-f)\sigma_1}\right)}\right)\right]^{n-1}\left[\frac{1}{3}d\epsilon_{\tilde{p}}\delta_{ij} + d\epsilon_{\tilde{q}}n_{ij}\right], \tag{11}$$

where $n_{ij} = \frac{3}{2}\frac{S_{ij}}{\tilde{q}}$ and $\dot{\epsilon}^T_{ij} = \dot{\epsilon}^e_{ij} + \dot{\epsilon}^c_{ij}$.

Equation (11) illustrates the relationship of the Rousselier damage model in a creep condition, where the parameter f of the void volume fraction will influence the existence of creep strain rate in the modeling of structural materials. This is the first contribution in ductile fracture damage analysis that introduced the void volume fraction f as a damage parameter in the creep modeling.

3 Creep crack growth modeling

Creep crack growth (CCG) is a principal failure mechanism of components operating at elevated temperature, thus requiring safe and accurate methods to predict such a reliability of components. The CCG analysis is performed to predict crack deformations and evaluate lifetime on the structural or component response. Nikbin et al. (1984) proposed the NSW model for the CCG based on the size of creep zone, which exists ahead of the crack tip damage accumulates, and creep damage was measured in terms of creep ductility exhaustion. This model considered that the material first experiences creep damage when it enters the process zone and the crack extends when the creep ductility exhausts at the crack tip. Nevertheless, the stress state ahead of the crack tip during the crack propagation was ignored in this model, which led to a conservative prediction. Therefore a modified NSW model was proposed, which considers the dependence of creep strain on both the crack tip angle Θ and

the creep stress exponent n, in addition to the stress state of the crack tip (Yatomi et al. 2008; Zhao et al. 2012).

The crack tip opening displacement (CTOD) method was implemented in compact-tension (CT) specimens for CCG for a Ni-base superalloy at 700 °C (Xia et al. 1996), Alloy 718 at 923 K, and austenitic stainless steel 0Cr18Ni9 at 550 °C (Chen et al. 2011). This method was used to control the crack extension when the CTOD value becomes equal to the critical values. The crack tip was allowed to advance by one element, and the stepwise was repeated until it reached maximum crack length. This method was capable of measuring at a specific distance from the crack tip and the amount of crack growth.

A special algorithm called the "Breakable element" was employed for the prediction of the crack growth in a solid subject to combined thermoelastic-plastic-creep load (Hsu and Zhai 1984). The versatility of this concept provides detailed stress and strain distributions, the kinematics of the inelastic zones, and the profile of the crack growth. Moreover, a modified creep ductility exhaustion model called the Manjoine multiaxial creep was conducted for numerical analysis of CCG in 316 stainless steel at 600 °C (Wen et al. 2013). This model crack growth was calculated by adding up the length of each completely damaged element ahead of the crack tip.

In the last decade, XFEM was used as an effective model to provide advantages in creep crack growth study, which has been discussed in the next section. From the previous application, the XFEM was used to simulate the creep crack growth in CT and CTS for P91 steel and 316 stainless steel at high temperature (Pandey et al. 2019). Also, the XFEM was implemented to model crack and crack growth behavior in the power-law of creep materials (Meng and Wang 2014). In XFEM, with the enrichment of the crack tip, the basic FE element may get converted into a tip element before it is converted into a split element. Therefore the element type may change as the crack grows (Kanth et al. 2020).

3.1 XFEM technique

This technique is numerical modeling of crack propagation where special functions are added to the finite element approximation using the partition of unity framework (Wang et al. 2016). The approximation for a displacement vector function **u** with the partition of unity enrichment is (Karmakov et al. 2020)

$$\mathbf{u} = \sum_{i=1}^{n} N_i(x) u_i + \sum_{j=1}^{m} N_j(x) H(\xi) a_j + \sum_{k=1}^{mt_1} N_k(x) \sum_{\alpha=1}^{mf} F_\alpha^1(x) b_k^{\alpha 1}$$

$$+ \sum_{k=1}^{mt_2} N_k(x) \sum_{\alpha=1}^{mf} F_\alpha^2(x) b_k^{\alpha 2}, \tag{12}$$

where $N_i(x)$ is the nodal shape function, $N_j(x)$ and $N_k(x)$ are the new set of shape functions associated with the enrichment part of the approximation, u_i is the nodal displacement vector associated with the continuous part of the finite element solution, $H(\xi)$ represents a discontinuous jump function across the crack surfaces, a_j, $b_k^{\alpha 1}$, and $b_k^{\alpha 2}$ are the enriched nodal degree of freedom vector for modeling crack faces and two crack tips, respectively, n is the number of nodes for each finite element, and m is the set of nodes that have the crack face (but excludes the crack tip) in their support domain, whereas mt_1 and mt_2 are the sets of nodes associated with crack tips 1 and 2 in their influence domain, and $F_\alpha^i(x)$, $i = 1, 2$, represent mf as the crack tip enrichment functions. Theoretically, the first term applies to all

nodes in the model, and the second term is for nodes whose shape functions support cross by the crack faces. Meanwhile, the third and fourth terms are only for nodes crossing at the crack tip.

The Heaviside function $H(\xi)$ across the crack surfaces can be defined as a sign function:

$$H(\xi) = \begin{cases} 1 & \text{if} \quad \xi \geq 0, \\ -1 & \text{otherwise,} \end{cases} \tag{13}$$

where $\xi = n.(x - x^*)$, is the local axis perpendicular to the crack growth direction, x is a Gauss point, x^* is the point on the crack closest to x, and n is the unit outward normal to the crack at x. Moreover, the isotropic asymptotic crack tip function $F_\alpha(r, \theta)$ is given as

$$F_\alpha(x) = \sqrt{r} \left[\sin \frac{\Theta}{2}, \cos \frac{\Theta}{2}, \sin \Theta \sin \frac{\Theta}{2}, \sin \Theta \cos \frac{\Theta}{2} \right], \tag{14}$$

where (r, Θ) is the polar coordinate system with its origin at the crack tip.

It should be noted that for XFEM elements, the location and the number of Gauss points between load increments may be changed as the crack propagates. Hence the material state variables must be updated consistently until the end of the load increment. However, in crack propagation problems, the crack crosses over a whole element allowing it to work on plane problems with a reduced integration element, so that the stresses and strains are calculated in the center of the element (on the integration point). Also, if the crack tip is not within an element, then the singularity of the stresses does not need to be considered in the definition of the elemental displacements (Serna Moreno et al. 2015). Therefore the crack must propagate across an entire element to avoid the need to model the stress singularity. Thus in the crack propagation of plane problem the XFEM discontinuous displacement approximation becomes

$$\mathbf{u} = \sum_{i=1}^{n} N_i(x) u_i + \sum_{j=1}^{m} N_j(x) H(\xi) a_j. \tag{15}$$

In the computational simulation of the XFEM formulation, the initiation and direction of the crack extension have to be defined to simulate the degradation and eventual failure of an enriched element. The failure mechanism consists of two notions, a crack initiation criterion and a damage evolution law. A crack process begins when the stresses or the strains (based on the damage of traction-separation law) satisfy specified crack initiation criteria. After that, the damage evolution law (based on the displacement or energy release rate criterion) describes the rate at which the cohesive stiffness is degraded once the corresponding initiation criterion is reached.

4 Numerical framework

Since the last half-century, the finite element method is among the computational technique that has successfully been used to analyze structures either in linear or nonlinear inelastic behavior. The selection of the integration scheme is necessary for the accuracy and stability of a solution, especially for nonlinear problems. Among many algorithms proposed in the literature, the return mapping method is effective, robust, unconditionally stable, and the most widely used for the problems involving plane strain and three-dimensional classical J_2 elastoplasticity.

This algorithm is based on the elastic predictor–plastic corrector, initially introduced in 1969 by Wilkins (1969). After several decades, Aravas (1987) proposed a framework of the radial return algorithm with Gurson's constitutive model by including the first invariant for the hydrostatic stress into the corrector part. Furthermore, he also provided a formula for calculating the consistent tangent moduli (CTM). Zhang (1995a,b) continued the modification by developing an explicit expression for the linearization moduli, which is close to the point return mapping algorithm. Resulting from this solution, no matrix inversion is therefore required to formulate the CTM expression. Arun et al. (2017) continues this significant work by implementing the return mapping method with a continuum damage model for a large-scale bending test on a welded steel pipe. Besides, Ahmad et al. proposed a new constitutive model based on the return mapping method algorithm for predicting the void damage-crack (Ahmad et al. 2019) and 3D model for aluminum wingbox aircraft structure (Ahmad et al. 2018).

In this study, the numerical integration of the constitutive model relations is performed using the Aravas–Zhang formulation (Bensaada et al. 2016; Zhang and Niemi 1995). In the subroutine the integration scheme uses the radial return algorithm, and an implicit solution method is formulated in the finite element method. The mathematical technique that implements the stress update algorithm is reviewed for the pressure-dependent viscoplasticity model based on the radial return method concept. For introducing the yield potential based on the formation of void growth, the Rousselier model is used in the analysis. Meanwhile, for creep material behavior, the Robinson model is revealed. Therefore the combination of both models generates a new modification called the MRR model, which is able to predict the creep damage behavior of the material with respect to void growth formation as a damage parameter.
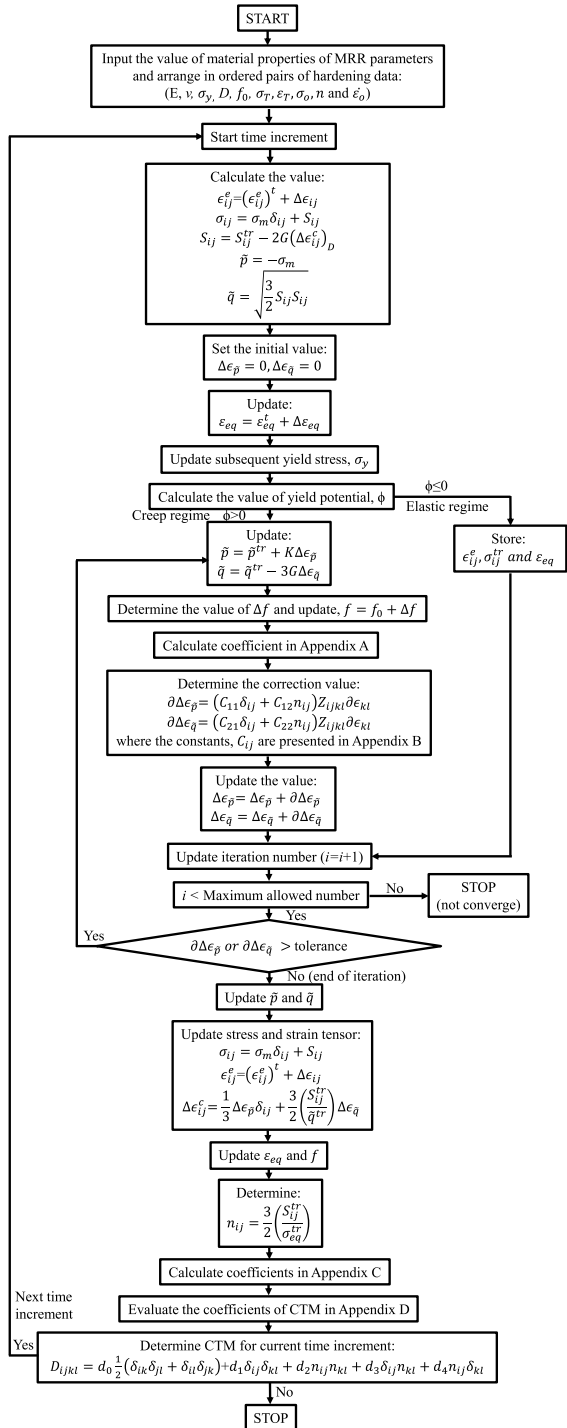
The MRR model is implemented using an Abaqus UMAT subroutine, which acts as an interface. To revise the algorithm process involved, the schematic flow diagram for the MRR model is presented in Fig. 1. The UMAT subroutine is the user-defined material of the ABAQUS/Standard module, which implements the implicit integration scheme to update the model state. For integration of the viscoplastic constitutive equation, the radial return algorithm (Aravas 1987; Zhang 1995a) is implemented involving two main parts, the elastic predictor part and the plastic corrector part. By exact linearization of the algorithm and decomposition of stresses into hydrostatic and deviatoric parts, a radial return mapping algorithm has been developed for generalized pressure-dependent viscoplasticity models. To solve the nonlinear equations of the increment of the stress tensor and the evolution of the internal variables model, the Newton–Raphson method based on Taylor series expansion is suggested (the derivations are shown in Appendix G). An implicit method has been formulated for finite element solution from static equilibrium, and the solution is determined iteratively until a convergence criterion is satisfied for each increment.
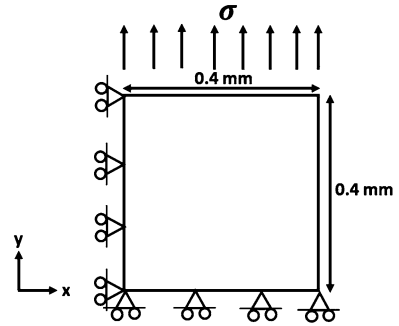
5 Data availability statement

The data supporting the findings of this study are available on request from the corresponding author, [etheses online submission: https://etheses.whiterose.ac.uk/23930/]. The data are not publicly available due to the contained information that could compromise the privacy of research findings.

Fig. 1 Schematic flow diagram of UMAT subroutine algorithm for MRR model

START

Input the value of material properties of MRR parameters and arrange in ordered pairs of hardening data:
$(E, \nu, \sigma_y, D, f_0, \sigma_T, \varepsilon_T, \sigma_o, n \text{ and } \dot{\varepsilon_o})$

Start time increment

Calculate the value:
$$\epsilon_{ij}^e = (\epsilon_{ij}^e)^t + \Delta\epsilon_{ij}$$
$$\sigma_{ij} = \sigma_m \delta_{ij} + S_{ij}$$
$$S_{ij} = S_{ij}^{tr} - 2G(\Delta\epsilon_{ij}^e)_D$$
$$\tilde{p} = -\sigma_m$$
$$\tilde{q} = \sqrt{\frac{3}{2} S_{ij} S_{ij}}$$

Set the initial value:
$\Delta\epsilon_{\tilde{p}} = 0, \Delta\epsilon_{\tilde{q}} = 0$

Update:
$\varepsilon_{eq} = \varepsilon_{eq}^t + \Delta\varepsilon_{eq}$

Update subsequent yield stress, σ_y

Calculate the value of yield potential, ϕ

$\phi \leq 0$ Elastic regime

Creep regime $\phi > 0$

Update:
$$\tilde{p} = \tilde{p}^{tr} + K\Delta\epsilon_{\tilde{p}}$$
$$\tilde{q} = \tilde{q}^{tr} - 3G\Delta\epsilon_{\tilde{q}}$$

Store:
$\epsilon_{ij}^e, \sigma_{ij}^{tr}$ and ε_{eq}

Determine the value of Δf and update, $f = f_0 + \Delta f$

Calculate coefficient in Appendix A

Determine the correction value:
$$\partial\Delta\epsilon_{\tilde{p}} = (C_{11}\delta_{ij} + C_{12}n_{ij})Z_{ijkl}\partial\epsilon_{kl}$$
$$\partial\Delta\epsilon_{\tilde{q}} = (C_{21}\delta_{ij} + C_{22}n_{ij})Z_{ijkl}\partial\epsilon_{kl}$$
where the constants, C_{ij} are presented in Appendix B

Update the value:
$$\Delta\epsilon_{\tilde{p}} = \Delta\epsilon_{\tilde{p}} + \partial\Delta\epsilon_{\tilde{p}}$$
$$\Delta\epsilon_{\tilde{q}} = \Delta\epsilon_{\tilde{q}} + \partial\Delta\epsilon_{\tilde{q}}$$

Update iteration number ($i = i+1$)

$i <$ Maximum allowed number

No → STOP (not converge)

Yes

Yes

$\partial\Delta\epsilon_{\tilde{p}}$ or $\partial\Delta\epsilon_{\tilde{q}} >$ tolerance

No (end of iteration)

Update $\tilde{p}$ and $\tilde{q}$

Update stress and strain tensor:
$$\sigma_{ij} = \sigma_m \delta_{ij} + S_{ij}$$
$$\epsilon_{ij}^e = (\epsilon_{ij}^e)^t + \Delta\epsilon_{ij}$$
$$\Delta\epsilon_{ij}^c = \frac{1}{3}\Delta\epsilon_{\tilde{p}}\delta_{ij} + \frac{3}{2}\left(\frac{S_{ij}^{tr}}{\tilde{q}^{tr}}\right)\Delta\epsilon_{\tilde{q}}$$

Update ε_{eq} and f

Determine:
$$n_{ij} = \frac{3}{2}\left(\frac{S_{ij}^{tr}}{\sigma_{eq}^{tr}}\right)$$

Calculate coefficients in Appendix C

Next time increment

Evaluate the coefficients of CTM in Appendix D

Yes

Determine CTM for current time increment:
$$D_{ijkl} = d_0 \frac{1}{2}(\delta_{ik}\delta_{jl} + \delta_{il}\delta_{jk}) + d_1\delta_{ij}\delta_{kl} + d_2 n_{ij}n_{kl} + d_3\delta_{ij}n_{kl} + d_4 n_{ij}\delta_{kl}$$

No

STOP

Fig. 2 2D-element under tension problem

Table 1 Mechanical properties and Rousselier parameters of 22 NiMoCr 3 7 steel material at 220 °C (Bass et al. 1993; Arun et al. 2017)

Young modulus E (GPa)	198
Poisson ratio v	0.3
Yield strength σ_y (MPa)	495
Rousselier parameter σ_1 (MPa)	578
Rousselier parameter D	2.62
Initial void volume fraction f_o	0.0005

6 Numerical verification of subroutines

6.1 A single 2D-plane strain element under tension

To verify the correctness of the MRR formulation in the subroutine codes, a simple uniaxial test is conducted based on a plane strain element with an element size of 0.4×0.4 mm^2. A four-node linear element is used in the FE analysis, and the loading and boundary condition are shown in Fig. 2. The mechanical properties of the tested material are given in Table 1. The exact solution of the problem is numerically obtained by Arun (2015) based on the suggestion from Aravas (1987) and Zhang (1994). The forward Euler integration is used in the solution, and the related differential equations for describing this problem are shown in Appendix E. To ensure the accuracy of the exact solution, the integration is performed from the initial yield strain to a strain of 1.0 using 200,000 increments (Arun 2015).

The results between the MRR subroutine solution and the exact solution are obtained and plotted as shown in Figs. 3 and 4. From these figures the results data are compared in terms of the values of the stresses and the void volume fractions as functions of the logarithmic strains. Both results follow the same patterns of the graphs, thus proving that the calculation in subroutine codes formulation is in correct condition and capable of solving the FE analysis problem.

6.2 A single 3D-solid element under tension

The verification test for the MRR subroutine is continued by considering a solid element in tension with an element size of $0.4 \times 0.4 \times 0.4$ mm^3. An eight-node solid element is used to model this test, and the loading and boundary condition are shown in Fig. 5. The mechanical properties are taken to be the same as those used in the previous problem (as shown in Table 1).

The integrated equations involve a numerically similar approach to the previous section and is reviewed in Appendix F. The results between the Rousselier subroutine and exact
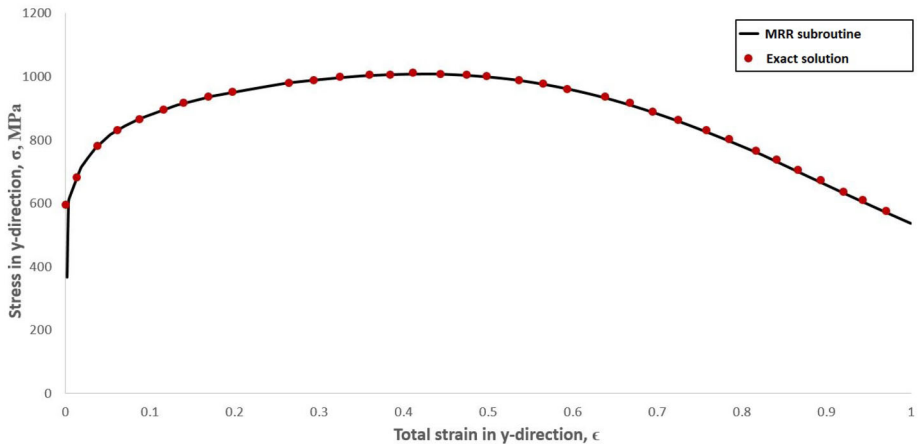
Fig. 3 Stress in y-direction as a function of total strain in y-direction
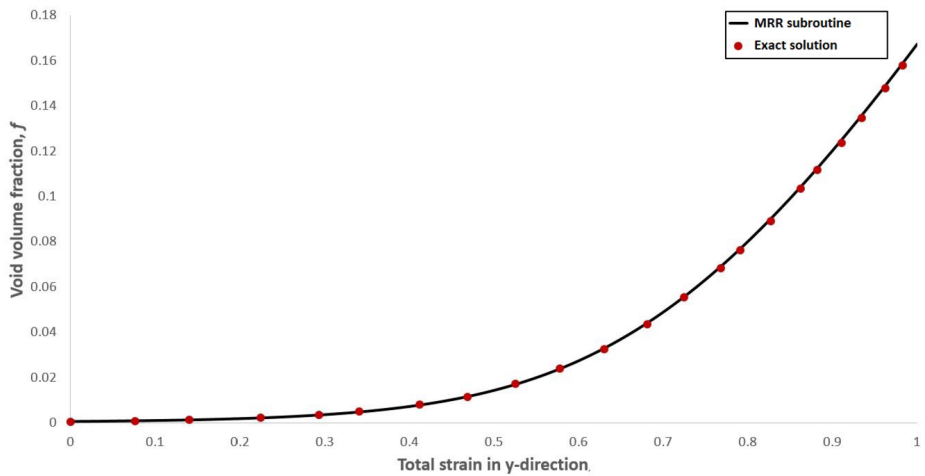
Fig. 4 Void volume fraction as a function of total strain in y-direction

solution for the stresses, the equivalent plastic strain and void volume fraction as functions of the logarithmic strain are plotted in Figs. 6 and 7, respectively. Thus these results show that a good agreement has been achieved between both solutions. Therefore the formulation of the subroutine codes is successfully verified for the development of the nonlinear numerical framework in the MRR model.

7 Computational test

7.1 Smooth tensile bar specimen

Tensile creep tests on smooth bars are modeled and replicated from the experimental work by Gaffard et al. (2005). A material selected for the specimen is a tempered martensitic

Fig. 5 3D-element under tension problem
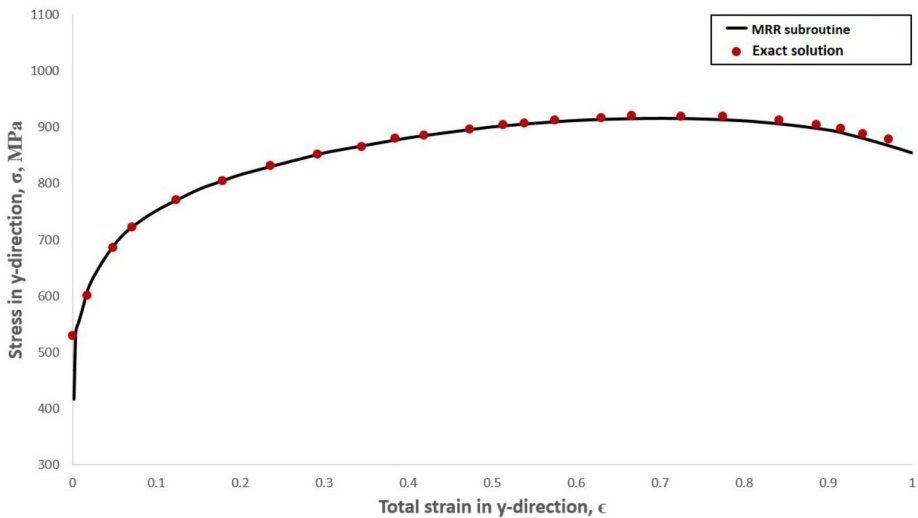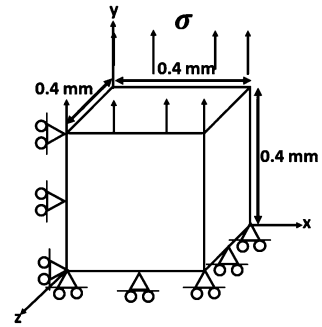
Fig. 6 Stress in y-direction as a function of total strain in y-direction

stainless steel of type 9Cr1Mo-NbV (P/T91) with a diameter of 10 mm and a gauge length of 50 mm. The specimens are tested at a constant temperature of 625 °C with different stress values of 100, 110, and 120 MPa, respectively. Due to the symmetrical geometry of the specimen, only one-quarter dimension has been considered for the analysis, and the geometry representation of the specimen can be referred to as shown in Fig. 8. Moreover, detailed information about the mechanical properties, the Robinson and Rousselier parameter constants of the material specimen are listed in Table 2, and hardening properties of the material are given in Table 3.

As a result, the contour distributions in the tensile specimen exerted by 120 MPa load are shown in Figs. 10, 11, and 12 with respect to the contour of von Mises stress, creep strain, and void volume fraction, respectively. Notice that in Figs. 10 the maximum value of stress concentration appeared near the center of the tensile specimen where the necking process takes place. A similar situation is in Fig. 11, in which the maximum creep strain value is stated around 12% near the center of the tensile specimen, where the strain is localized in this necking region. In addition, the contour distribution of void volume fraction f is also presented in Fig. 12, which indicates a critical value of void volume fraction of 0.01 near the center of the tensile specimen. This critical value is reportedly similar to the significant
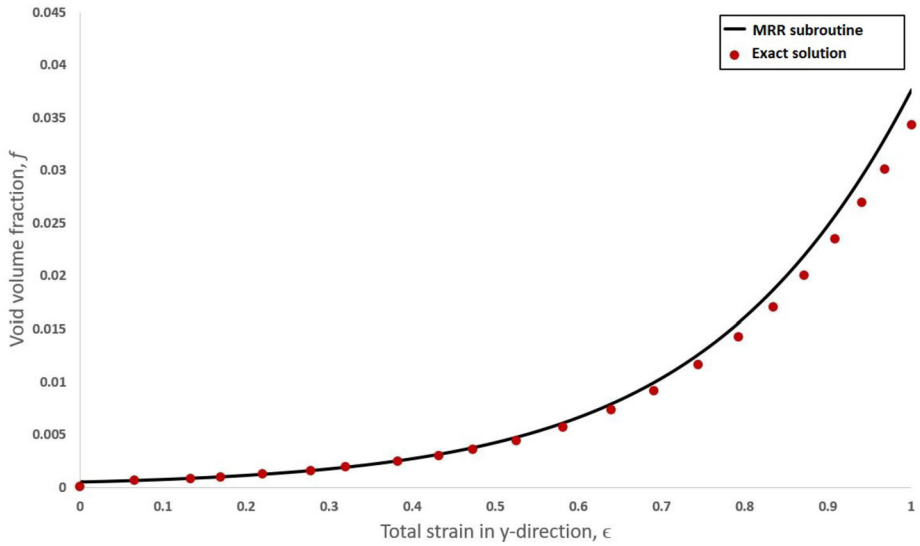
**Fig. 7** Void volume fraction as a function of total strain in y-direction

Fig. 8 Geometry representation
for smooth tensile bar specimen
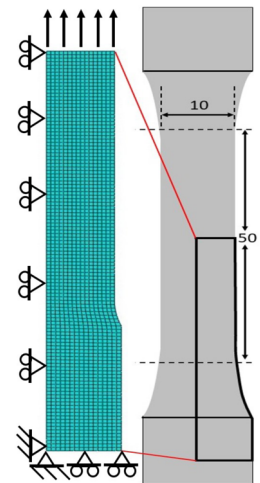
value mentioned in the literature (Samal et al. 2010). The decomposition of the void volume fraction is contributed to the overall damage growth in the tensile specimen and based on the experimental evidence that damage does not occur before the onset of necking (Gaffard et al. 2005). Again, as the stress concentration is maximum at the center of the tensile specimen, void growth also tends to be maximum in this region.

For further analysis, an element is chosen based on a critical position during a test, as illustrated in Fig. 9. Thus Fig. 13 displays the creep strain component as a function of void volume fraction at different stresses. The void growth that represents the creep damage growth of the tensile specimen enhanced the creep strain development promptly. The highest applied stress might also influence the existence of voids growth with the formation of the creep strain. A creep damage structure initially incurs void damage in regions of relatively

Fig. 9 Element position for a detailed analysis
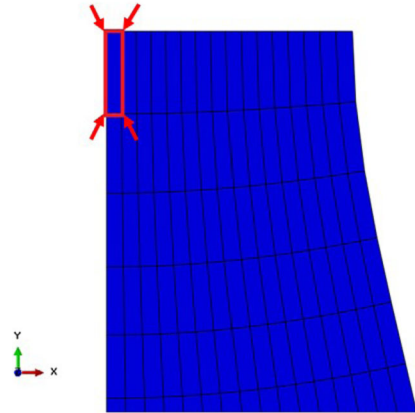
Table 2 Mechanical properties and Rousselier parameters of tempered martensitic stainless steel, 9Cr1Mo-NbV (P/T91) at 625 °C (Gaffard et al. 2005; Tvergaard and Needleman 1984)

|	
Young modulus E (GPa)	145
Poisson ratio v	0.3
Yield strength σ_y (MPa)	340
Rousselier parameter σ_1 (MPa)	238
Rousselier parameter D	2
Initial void volume fraction f_o	0.0002
Reference stress σ_o (MPa)	100
Robinson creep parameter $\dot{\varepsilon}_o$ (s^{-1})	0.0011
Robinson creep parameter n	11

Table 3 Hardening data of tempered martensitic stainless steel, 9Cr1Mo-NbV (P/T91) at 625 °C (Gaffard et al. 2005; Tvergaard and Needleman 1984)

True strain ϵ_T	True stress σ_T (MPa)
0.257	345.5
0.286	350
0.343	354.5
0.457	363.6
0.571	372.7
0.686	381.8
0.829	400
1.029	409.1

high strain, leading to local softening and subsequent redistribution of strain as the damage zone spreads throughout the structure.

The structure analysis is continued by identifying the evolution of void volume fraction with time in different applied stresses, as shown in Fig. 14. It can be seen in the graph that the highest value of applied stress (120 MPa) influences the time period of loading to a shorter time for the specimen to reach a critical void damage growth of the tensile specimen. As mentioned before, the specimen shows a maximum value of the voids damage fraction at the center of the specimen that is in the necking region. Critical damage is only observed after a necking process and induced due to increased stress triaxiality and creep strain effects. To make sure that the MRR model well describes the void damage growth in creep flow,
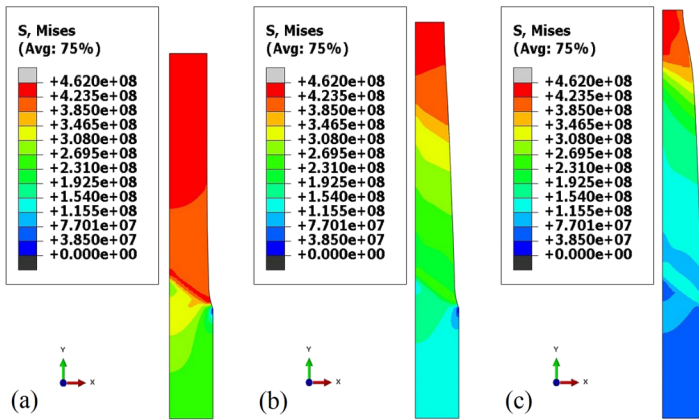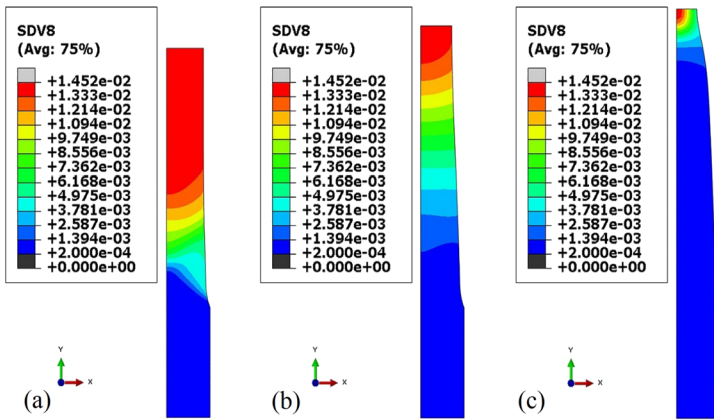
**Fig. 10** Contour of von Mises stress in the specimen of loading 120 MPa at (**a**) $t = 300$ h, (**b**) $t = 600$ h, and (**c**) $t = 886$ h
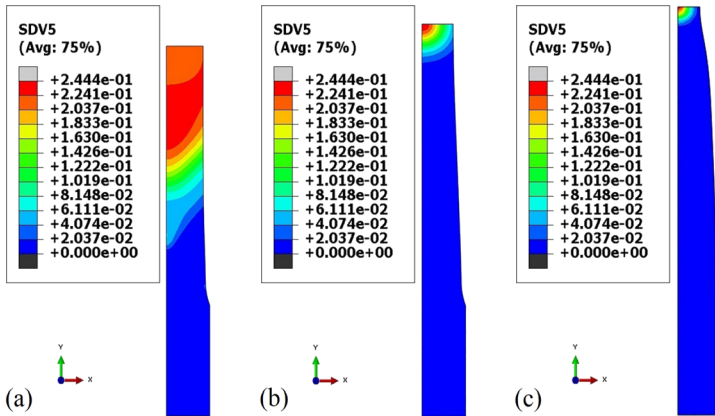
Fig. 11 Contour of creep strain of specimen of loading 120 MPa at (**a**) $t = 300$ h, (**b**) $t = 600$ h, and (**c**) $t = 886$ h

the result has been compared to the other solution of the Norton-GTN model by Samal et al. (2010) at 110 MPa. This validation strategy has proven that a good agreement has been achieved between both models to estimate the void damage growth and satisfactorily predicts the time to failure.

Last but not least, Fig. 15 illustrates the creep strain curves over time along with experimental data (Gaffard et al. 2005) in different stresses. We can see from Fig. 15 that the creep damage model developed in this work was able to successfully predict the creep strain behavior from the experimental for all kinds of stresses. As expected, the creep strain curves are found dominantly by the tertiary creep stage, which involves the material rupture life, and it is mostly due to softening effects. The MRR model has a lot of potentials to predict the long-term creep damage behavior of the materials. As long-term creep tests are expensive and time-consuming, this solution model can fill the gap for solving complex structural problems in the engineering field.

Fig. 12 Contour of void volume fraction of specimen of loading 120 MPa at (**a**) $t = 300$ h, (**b**) $t = 600$ h, and (**c**) $t = 886$ h
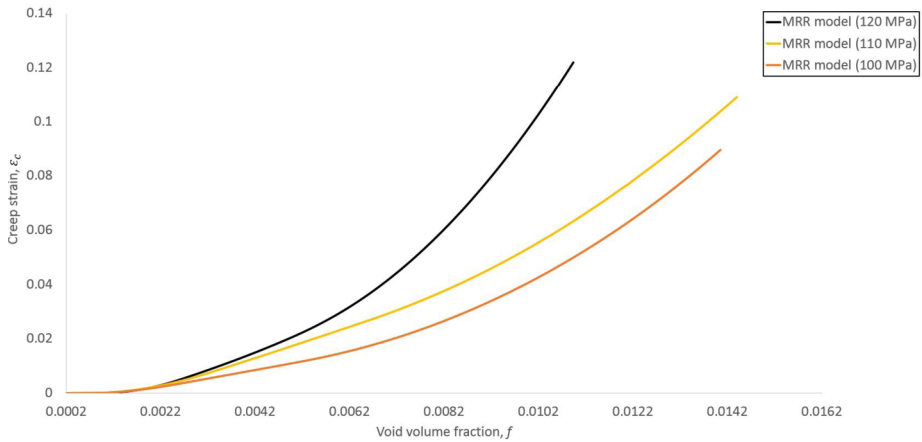
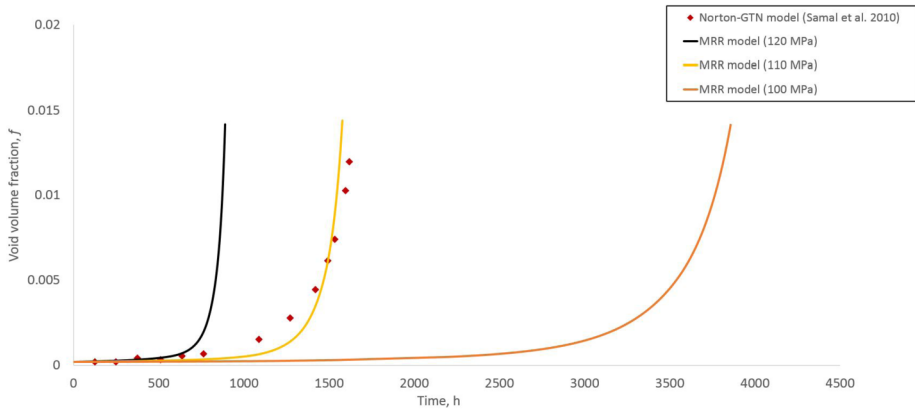**Fig. 13** Creep strain vs void volume fraction f for the tensile specimen at different stresses

8 MRR model with crack development based on XFEM

This structural analysis is extended by introducing the tensile specimen crack development based on the XFEM technique. The XFEM and MRR models are used in the numerical modeling of creep damage, which works to establish the connection between the tensile specimen void and crack growth by inventing a new model called the modified Robinson–Rousselier XFEM (MRRX) model. The developed MRRX model promises a proper solution technique for predicting the creep damage behavior in terms of the micromechanical damage due to void and crack development in the material structure.

Figures 16 and 17 show the contour distribution of the stress in the y-direction and void volume fraction damage along with the crack propagation near the center of the tensile specimen. We can observe from Fig. 17 that the voids damage grows at zones of high stress (as shown in Fig. 16), which is at the crack tip region. Damage results in softening of the material and fracture proceed from the competition between hardening and damage. When
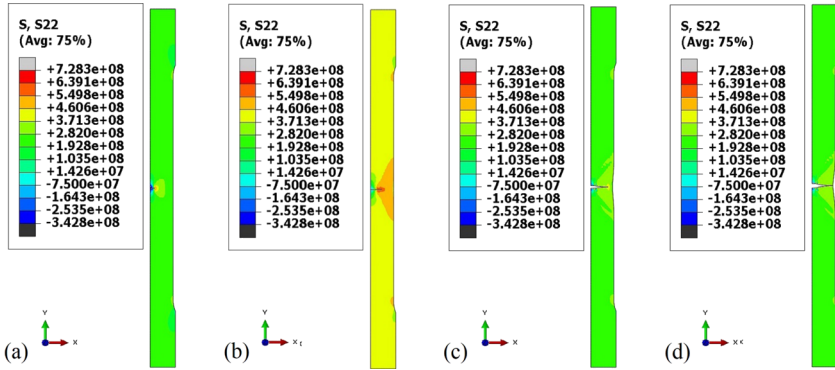
Fig. 14 Evolution of void volume fraction f in MRR model loaded at different stresses and comparison with Norton-GTN model results at 110 MPa
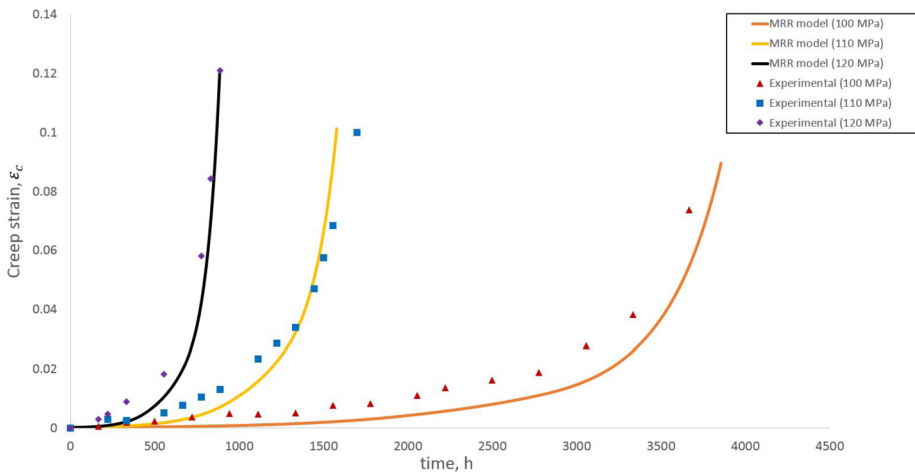

Fig. 15 Comparison of experimental and simulation results of creep strain curves for the tensile specimen at different stresses

damage overcomes the hardening of the material at the tip of a crack, there is strain localization, which rapidly results in tremendous strains and damage. The stresses decrease abruptly and vanish, and the zone of strain and damage localization can be assimilated to a crack.

Furthermore, the evolution of crack growth is visualized in some detail with the formation of voids growth in the crack path as shown in Fig. 18, and the results are compared with the results found in the literature (Tvergaard and Needleman 1984), which is shown in Fig. 19. By considering a similar pattern of the crack growth behavior between both techniques (Figs. 18 and 19) the characterization of crack starts with (a) the initiation of the crack and formation of void damage in the crack-tip of the specimen; (b) and (c) specimen forms a yield plastically due to increasing of stress and damage formation near to the crack-tip, and the void forms a shear band due to the influence of shear localization; (d) and (e) the evolution is extended as the voids coalesce along with the shear bands and the crack growth

Fig. 16 Contour distribution of stress in the y-direction along the crack near the center of the tensile specimen at (**a**) $t = 13$ h, (**b**) $t = 22$ h, (**c**) $t = 84$ h, and (**d**) $t = 129$ h
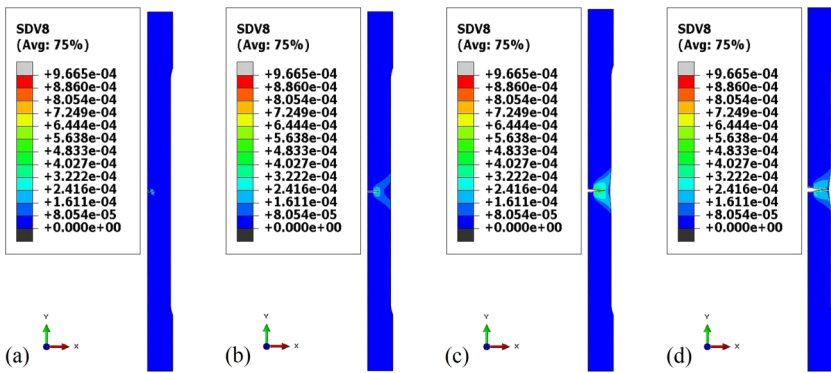

Fig. 17 Contour distribution of void volume fraction, f along the crack near the center of the tensile specimen at (**a**) $t = 13$ h, (**b**) $t = 22$ h, (**c**) $t = 84$ h, and (**d**) $t = 129$ h

continues along the surface; (f) the strength of the structure is lost due to a final crack or called the ultimate fracture mode. Note that the degree of necking observed on a specimen is a function of the nucleation and failure laws for the particular material, since necking essentially stops when the crack initiates.

In addition, it is mentioned in Tvergaard and Needleman (1984) that from the calculation it was not able to conclude whether the zig-zag of the crack propagation exhibited in Fig. 19 is real or it is just a mesh effect. They also claimed that this scenario is due to the feature of the cup-cone fracture process of the tensile specimen. However, these statements create some arguments with the current results in this analysis, as shown in Fig. 18. There are no zig-zag signs of the crack appear in Fig. 18, and only the crack propagates across the center of the tensile specimen parallel to the crack tip area. Thus we believe that the zig-zag formed in the previous results is due to the effect of the mesh in FE and is not because of the features of the bifurcation or cup-cone fracture. This statement can be strongly supported and well explained by the previous literature (Ahmad et al. 2019).

Fig. 18 Evolution of cracks growth near the center of tensile specimen based on XFEM technique
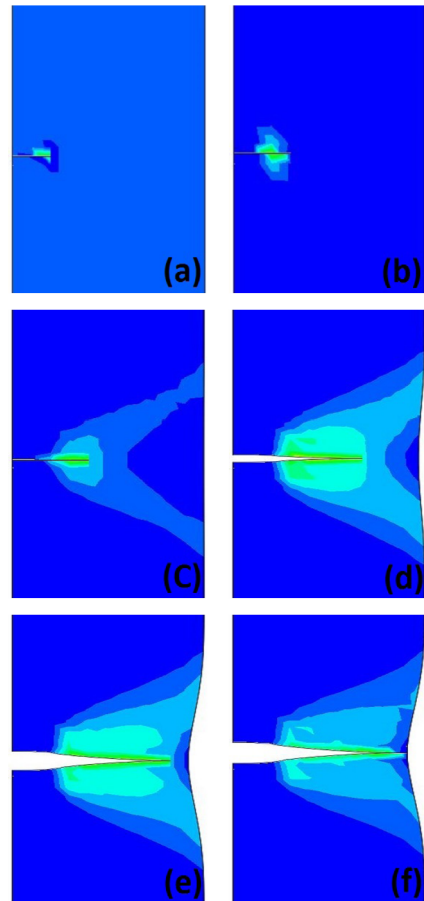

9 Conclusion

In this study, we developed a micromechanical creep damage model to simulate the deformation and damage development of the creep ductile materials. The proposed solution model, called the MRR model, has the potential to predict the creep behavior at different load levels with the existence of void growth for representing the damage parameter in this analysis. Some points need to be highlighted here:

– The MRR model formulation interface was implemented in the UMAT subroutine of the Abaqus/Standard module, which exhibits the implicit integration scheme to update the state of the model and the consistent tangent modulus required for developing the mechanical constitutive model. The radial return mapping method was executed for introducing the integration of the elastoplastic constitutive relations. The Newton–Raphson method based on Taylor series expansion was suggested to solve the nonlinear equations of the increment of the stress tensor and the evolution of the internal variable model. The algorithms were addressed by an iterative method, and the static implicit was formulated as a solution method in this study.

– Tensile creep tests on smooth bars were carried out to identify the capability of the MRR model to predict the creep damage behavior of P91 steel. The specimen was loaded in

Fig. 19 Evolution of cracks growth near the center of tensile specimen based on the element-vanish technique (Tvergaard and Needleman 1984)
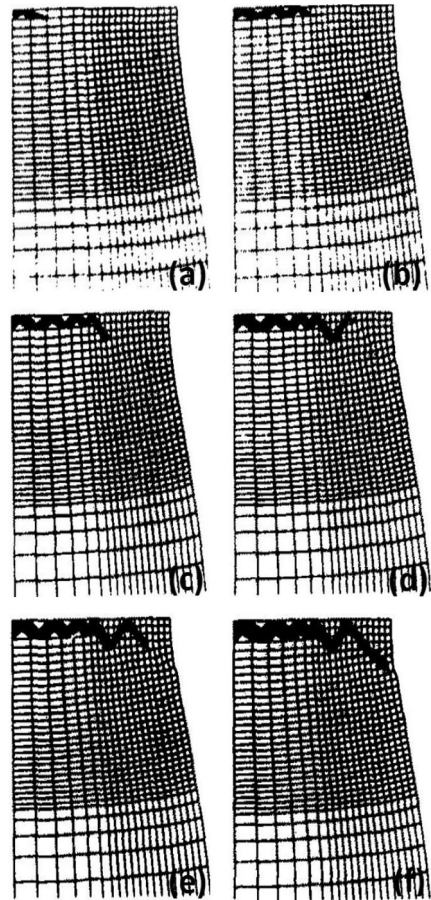
different stress levels (100–120 MPa) to see the variations of the results and recognize the effect of applied stress in the formation of damage, creep strain, and lifetime of the specimen. The results found that the maximum value of stress, creep strain, and void damage was detected near the center of the tensile specimen where the necking process was formed. Then the simulation results were compared with the experimental data and showed that a good reasonable agreement was achieved between both results. The MRR model has successfully estimated the void damage growth, the creep strain curve, and the time to failure of the material. The influences of the applied stresses toward the time period for reaching a critical void damage growth were also stated in this analysis. In addition, the authors claimed that this is the first work contribution that introduces the relation of void damage growth toward the formation of creep strain behavior in the material through the constitutive modeling.

– The MRR model analysis was extended for the crack development based on the XFEM technique. As a result, a new model, called the MRRX model, was introduced for predicting the creep damage behavior in terms of the micromechanical damage due to void and crack development in the material structure. The simulation results were compared with the literature solution with respect to the evolutions of the crack growth with void damage. A good comparison was achieved between both techniques, proving the potential of

the MRRX model to predict the creep damage behavior in terms of the void-crack growth in the ductile material structures.

For further investigation, the MRR model will be tested in the 3D-modeling problem, which involves a high degree of freedom and a complex integration solution in the analysis.

Appendix A: Coefficients of the correction value for volumetric and deviatoric creep strain

$$A_{11}d\Delta\epsilon_{\tilde{p}} + A_{12}d\Delta\epsilon_{\tilde{q}} = b_1, \tag{16}$$

$$A_{21}d\Delta\epsilon_{\tilde{p}} + A_{22}d\Delta\epsilon_{\tilde{q}} = b_2, \tag{17}$$

$$A_{11} = \tilde{P} + \Delta\epsilon_{\tilde{p}}\left(K\frac{\partial\tilde{P}}{\partial\tilde{p}} + \frac{\partial\tilde{P}}{\partial H^1}\frac{\partial H^1}{\partial\Delta\epsilon_{\tilde{p}}} + \frac{\partial\tilde{P}}{\partial H^2}\frac{\partial H^2}{\partial\Delta\epsilon_{\tilde{p}}}\right)$$
$$+ \Delta\epsilon_{\tilde{q}}\left(K\frac{\partial\tilde{Q}}{\partial\tilde{p}} + \frac{\partial\tilde{Q}}{\partial H^1}\frac{\partial H^1}{\partial\Delta\epsilon_{\tilde{p}}} + \frac{\partial\tilde{Q}}{\partial H^2}\frac{\partial H^2}{\partial\Delta\epsilon_{\tilde{p}}}\right), \tag{18}$$

$$A_{12} = \tilde{Q} + \Delta\epsilon_{\tilde{p}}\left(-3G\frac{\partial\tilde{P}}{\partial\tilde{q}} + \frac{\partial\tilde{P}}{\partial H^1}\frac{\partial H^1}{\partial\Delta\epsilon_{\tilde{q}}} + \frac{\partial\tilde{P}}{\partial H^2}\frac{\partial H^2}{\partial\Delta\epsilon_{\tilde{q}}}\right)$$
$$+ \Delta\epsilon_{\tilde{q}}\left(-3G\frac{\partial\tilde{Q}}{\partial\tilde{q}} + \frac{\partial\tilde{Q}}{\partial H^1}\frac{\partial H^1}{\partial\Delta\epsilon_{\tilde{q}}} + \frac{\partial\tilde{Q}}{\partial H^2}\frac{\partial H^2}{\partial\Delta\epsilon_{\tilde{q}}}\right), \tag{19}$$

$$A_{21} = K\frac{\partial\phi}{\partial\tilde{p}} + \frac{\partial\phi}{\partial H^1}\frac{\partial H^1}{\partial\Delta\epsilon_{\tilde{p}}} + \frac{\partial\phi}{\partial H^2}\frac{\partial H^2}{\partial\Delta\epsilon_{\tilde{p}}}, \tag{20}$$

$$A_{22} = -3G\frac{\partial\phi}{\partial\tilde{q}} + \frac{\partial\phi}{\partial H^1}\frac{\partial H^1}{\partial\Delta\epsilon_{\tilde{q}}} + \frac{\partial\phi}{\partial H^2}\frac{\partial H^2}{\partial\Delta\epsilon_{\tilde{q}}}, \tag{21}$$

$$b_1 = -\Delta\epsilon_{\tilde{p}}\tilde{P} - \Delta\epsilon_{\tilde{q}}\tilde{Q}, \tag{22}$$

$$b_2 = -\phi, \tag{23}$$

where $\Delta\epsilon_{\tilde{p}}$ and $\Delta\epsilon_{\tilde{q}}$ are the volumetric and deviatoric creep strain increments, and H^i is the hardening of internal state variable.

Appendix B: Coefficients of the CTM expression

$$C_{11} = \left[\left(\bar{A}_{22} + 3GB_{22}\right)B_{11} - \left(\bar{A}_{12} + 3GB_{12}\right)B_{12}\right]/\Delta, \tag{24}$$

$$C_{12} = \left[\left(\bar{A}_{22} + 3GB_{22}\right)B_{12} - \left(\bar{A}_{12} + 3GB_{12}\right)B_{22}\right]/\Delta, \tag{25}$$

$$C_{21} = \left[\left(\bar{A}_{11} + 3KB_{11}\right)B_{21} - \left(\bar{A}_{21} + 3KB_{21}\right)B_{11}\right]/\Delta, \tag{26}$$

$$C_{22} = \left[\left(\bar{A}_{11} + 3KB_{11}\right)B_{22} - \left(\bar{A}_{21} + 3KB_{21}\right)B_{12}\right]/\Delta, \tag{27}$$

$$\Delta = \left(\bar{A}_{11} + 3KB_{11}\right)\left(\bar{A}_{22} + 3GB_{22}\right) - \left(\bar{A}_{12} + 3GB_{11}\right)\left(\bar{A}_{21} + 3KB_{21}\right), \tag{28}$$

where G and K are the elastic shear and bulk modulus.

Appendix C: Coefficient of the linearization of the flow and yield condition

$$\bar{A}_{11} \partial \Delta \epsilon_{\tilde{p}} + \bar{A}_{12} \partial \Delta \epsilon_{\tilde{q}} = \left(B_{11} \delta_{ij} + B_{12} n_{ij} \right) \partial \sigma_{ij}, \tag{29}$$

$$\bar{A}_{21} \partial \Delta \epsilon_{\tilde{p}} + \bar{A}_{22} \partial \Delta \epsilon_{\tilde{q}} = \left(B_{21} \delta_{ij} + B_{22} n_{ij} \right) \partial \sigma_{ij}, \tag{30}$$

where

$$\bar{A}_{11} = \tilde{P} + \Delta \epsilon_{\tilde{p}} \left(\frac{\partial \tilde{P}}{\partial H^1} \frac{\partial H^1}{\partial \Delta \epsilon_{\tilde{p}}} + \frac{\partial \tilde{P}}{\partial H^2} \frac{\partial H^2}{\partial \Delta \epsilon_{\tilde{p}}} \right) + \Delta \epsilon_{\tilde{q}} \left(\frac{\partial \tilde{Q}}{\partial H^1} \frac{\partial H^1}{\partial \Delta \epsilon_{\tilde{p}}} + \frac{\partial \tilde{Q}}{\partial H^2} \frac{\partial H^2}{\partial \Delta \epsilon_{\tilde{p}}} \right), \tag{31}$$

$$\bar{A}_{21} = \frac{\partial \phi}{\partial H^1} \frac{\partial H^1}{\partial \Delta \epsilon_{\tilde{p}}} + \frac{\partial \phi}{\partial H^2} \frac{\partial H^2}{\partial \Delta \epsilon_{\tilde{p}}}, \tag{32}$$

$$\bar{A}_{22} = \frac{\partial \phi}{\partial H^1} \frac{\partial H^1}{\partial \Delta \epsilon_{\tilde{q}}} + \frac{\partial \phi}{\partial H^2} \frac{\partial H^2}{\partial \Delta \epsilon_{\tilde{q}}}, \tag{33}$$

$$B_{11} = \frac{\Delta \epsilon_{\tilde{p}}}{3} \left(\frac{\partial \tilde{P}}{\partial \tilde{p}} + \frac{\partial \tilde{P}}{\partial H^1} \frac{\partial H^1}{\partial \tilde{p}} + \frac{\partial \tilde{P}}{\partial H^2} \frac{\partial H^2}{\partial \tilde{p}} \right) + \frac{\Delta \epsilon_{\tilde{q}}}{3} \left(\frac{\partial \tilde{Q}}{\partial \tilde{p}} + \frac{\partial \tilde{Q}}{\partial H^1} \frac{\partial H^1}{\partial \tilde{p}} + \frac{\partial \tilde{Q}}{\partial H^2} \frac{\partial H^2}{\partial \tilde{p}} \right), \tag{34}$$

$$B_{12} = -\Delta \epsilon_{\tilde{p}} \left(\frac{\partial \tilde{P}}{\partial \tilde{q}} + \frac{\partial \tilde{P}}{\partial H^1} \frac{\partial H^1}{\partial \tilde{q}} + \frac{\partial \tilde{P}}{\partial H^2} \frac{\partial H^2}{\partial \tilde{q}} \right) - \Delta \epsilon_{\tilde{q}} \left(\frac{\partial \tilde{Q}}{\partial \tilde{q}} + \frac{\partial \tilde{Q}}{\partial H^1} \frac{\partial H^1}{\partial \tilde{q}} + \frac{\partial \tilde{Q}}{\partial H^2} \frac{\partial H^2}{\partial \tilde{q}} \right), \tag{35}$$

$$B_{21} = \frac{1}{3} \left(Q + \frac{\partial \phi}{\partial H^1} \frac{\partial H^1}{\partial \tilde{p}} + \frac{\partial \phi}{\partial H^2} \frac{\partial H^2}{\partial \tilde{p}} \right), \tag{36}$$

$$B_{22} = - \left(P + \frac{\partial \phi}{\partial H^1} \frac{\partial H^1}{\partial \tilde{q}} + \frac{\partial \phi}{\partial H^2} \frac{\partial H^2}{\partial \tilde{q}} \right). \tag{37}$$

Appendix D: Five constants for the CTM explicit expression

$$d_0 = 2G \frac{\tilde{q}}{\tilde{q}^{tr}}, \tag{38}$$

$$d_1 = K - \frac{2G}{3} \frac{\tilde{q}}{\tilde{q}^{tr}} - 3K^2 C_{11}, \tag{39}$$

$$d_2 = \frac{4G^2}{\tilde{q}^{tr}} \Delta \epsilon_{\tilde{q}} - 4G^2 C_{22}, \tag{40}$$

$$d_3 = -2GK C_{12}, \tag{41}$$

$$d_4 = -6GK C_{21}. \tag{42}$$

Note that D_{ijkl} is symmetric if $C_{12} = 3C_{21}$.

Appendix E: The differential equations for a single 2D-plane strain element

$$\frac{d\epsilon_y^{\tilde{p}}}{d\epsilon_y} = \omega \left\{ -\frac{1}{3} \frac{\partial \phi}{\partial \left(\frac{\tilde{p}}{\rho} \right)} + \frac{\partial \phi}{\partial \left(\frac{S_y}{\rho} \right)} \right\}, \tag{43}$$

$$\frac{d\epsilon_z^{\tilde{p}}}{d\epsilon_y} = \omega \left\{ -\frac{1}{3} \frac{\partial \phi}{\partial \left(\frac{\tilde{p}}{\rho} \right)} + \frac{\partial \phi}{\partial \left(\frac{S_z}{\rho} \right)} \right\}, \tag{44}$$

$$\frac{d\sigma_y}{d\epsilon_y} = \frac{E}{(1-v^2)} \left\{ 1 - \frac{d\epsilon_y^{\tilde{p}}}{d\epsilon_y} - v \frac{d\epsilon_z^{\tilde{p}}}{d\epsilon_y} \right\}, \tag{45}$$

$$\frac{d\sigma_z}{d\epsilon_y} = v \frac{d\sigma_y}{d\epsilon_y} - E \frac{d\epsilon_z^{\tilde{p}}}{d\epsilon_y}, \tag{46}$$

$$\frac{d\varepsilon_{eq}}{d\epsilon_y} = \omega, \tag{47}$$

$$\frac{df}{d\epsilon_y} = \omega f D (1 - f) e^{\left(\frac{-\tilde{p}}{\rho \sigma_1} \right)}, \tag{48}$$

$$\omega = \frac{\frac{E}{(1-v^2)} \left(\frac{\partial \phi}{\partial \sigma_y} + v \frac{\partial \phi}{\partial \sigma_z} \right)}{\frac{E}{(1-v^2)} \left\{ \frac{\partial \phi}{\partial \sigma_y} \frac{\partial \phi}{\partial \left(\frac{\sigma_y}{\rho} \right)} + \frac{\partial \phi}{\partial \sigma_z} \frac{\partial \phi}{\partial \left(\frac{\sigma_z}{\rho} \right)} + v \frac{\partial \phi}{\partial \sigma_z} \frac{\partial \phi}{\partial \left(\frac{\sigma_y}{\rho} \right)} + v \frac{\partial \phi}{\partial \sigma_y} \frac{\partial \phi}{\partial \left(\frac{\sigma_z}{\rho} \right)} \right\} - \frac{\partial \phi}{\partial \varepsilon_{eq}} - \frac{\partial \phi}{\partial f} \frac{\partial f}{\partial \varepsilon_{eq}}}, \tag{49}$$

where E, v, and ϕ are Young's modulus, Poisson's ratio, and the plastic potential, ϵ_y, $\epsilon_y^{\tilde{p}}$, and $\epsilon_z^{\tilde{p}}$ are the total strain and creep strains in the y- and z-directions, and σ_y and σ_z are the components of stress in the y- and z-directions, respectively.

Appendix F: The differential equations for a single 3D-solid element

$$\frac{d\epsilon_y^{\tilde{p}}}{d\epsilon_y} = \bar{\omega} \left\{ -\frac{1}{3} \frac{\partial \phi}{\partial \left(\frac{\tilde{p}}{\rho} \right)} + \frac{\partial \phi}{\partial \left(\frac{S_y}{\rho} \right)} \right\}, \tag{50}$$

$$\frac{d\sigma_y}{d\epsilon_y} = E \left\{ 1 - \bar{\omega} \left[\frac{\partial \phi}{\partial \left(\frac{S_y}{\rho} \right)} - \frac{1}{3} \frac{\partial \phi}{\partial \left(\frac{p}{\rho} \right)} \right] \right\}, \tag{51}$$

$$\frac{d\varepsilon_{eq}^{\tilde{p}}}{d\epsilon_y} = \bar{\omega}, \tag{52}$$

$$\frac{df}{d\epsilon_y} = \bar{\omega} f D (1 - f) e^{\left(\frac{-\tilde{p}}{\rho \sigma_1} \right)}, \tag{53}$$

$$\bar{\omega} = \frac{E \frac{\partial \phi}{\partial \sigma_y}}{E \frac{\partial \phi}{\partial \sigma_y} \left\{ -\frac{1}{3} \frac{\partial \phi}{\partial \left(\frac{\tilde{p}}{\rho} \right)} + \frac{\partial \phi}{\partial \left(\frac{S_y}{\rho} \right)} \right\} - \frac{\partial \phi}{\partial \varepsilon_{eq}^{\tilde{p}}} - \frac{\partial \phi}{\partial f} \frac{\partial f}{\partial \varepsilon_{eq}^{\tilde{p}}}}, \tag{54}$$

where E is Young's modulus, ϵ_y and $\epsilon_y^{\tilde{p}}$ are the total and creep strains in the y-direction, and σ_y is the component of stress in the y-direction.

Appendix G: Integrating of nonlinear equation

Following to the Newton–Raphson method based on Taylor series expansion, $\Delta \epsilon_{\tilde{p}}$ and $\Delta \epsilon_{\tilde{q}}$ are used to formulate the internal variables of the model as (Aravas 1987)

$$0 = \Delta \epsilon_{\tilde{p}} \left(\frac{\partial \phi}{\partial \tilde{q}} \right) + \Delta \epsilon_{\tilde{q}} \left(\frac{\partial \phi}{\partial \tilde{p}} \right), \tag{55}$$

$$
\begin{aligned}
0 = \Delta \epsilon_{\tilde{p}} \tilde{P} + \Delta \epsilon_{\tilde{q}} \tilde{Q} + d \Delta \epsilon_{\tilde{p}} \left[\tilde{P} + \Delta \epsilon_{\tilde{p}} \frac{\partial \tilde{P}}{\partial \Delta \epsilon_{\tilde{p}}} + \Delta \epsilon_{\tilde{q}} \frac{\partial \tilde{Q}}{\partial \Delta \epsilon_{\tilde{p}}} \right] \\
+ d \Delta \epsilon_{\tilde{q}} \left[\tilde{Q} + \Delta \epsilon_{\tilde{p}} \frac{\partial \tilde{P}}{\partial \Delta \epsilon_{\tilde{q}}} + \Delta \epsilon_{\tilde{q}} \frac{\partial \tilde{Q}}{\partial \Delta \epsilon_{\tilde{q}}} \right] + d H^1 \left[\Delta \epsilon_{\tilde{p}} \frac{\partial \tilde{P}}{\partial H^1} + \Delta \epsilon_{\tilde{q}} \frac{\partial \tilde{Q}}{\partial H^1} \right] \\
+ d H^2 \left[\Delta \epsilon_{\tilde{p}} \frac{\partial \tilde{P}}{\partial H^2} + \Delta \epsilon_{\tilde{q}} \frac{\partial \tilde{Q}}{\partial H^2} \right],
\end{aligned} \tag{56}
$$

where $\tilde{P} = \frac{\partial \phi}{\partial \tilde{q}}$ and $\tilde{Q} = \frac{\partial \phi}{\partial \tilde{p}}$, whereas $\partial \Delta \epsilon_{\tilde{p}}$ and $\partial \Delta \epsilon_{\tilde{q}}$ are defined as the correction values for $\Delta \epsilon_{\tilde{p}}$ and $\Delta \epsilon_{\tilde{q}}$, respectively. Moreover, the values of $d H^1$ and $d H^2$ can be determined as follows:

$$\begin{bmatrix} d H^1 \\ d H^2 \end{bmatrix} = -\frac{1}{\Omega} \begin{bmatrix} E_1 & E_2 \\ E_3 & E_4 \end{bmatrix} \begin{bmatrix} d \Delta \epsilon_{\tilde{p}} \\ d \Delta \epsilon_{\tilde{q}} \end{bmatrix}, \tag{57}$$

where

$$\Omega = \left(\frac{\partial G^1}{\partial H^1} \right) \left(\frac{\partial G^2}{\partial H^2} \right) - \left(\frac{\partial G^2}{\partial H^1} \right) \left(\frac{\partial G^1}{\partial H^2} \right), \tag{58}$$

$$E_1 = \left(\frac{\partial G^2}{\partial H^2} \frac{\partial G^1}{\partial \Delta \epsilon_{\tilde{p}}} - \frac{\partial G^1}{\partial H^2} \frac{\partial G^2}{\partial \Delta \epsilon_{\tilde{p}}} \right) + \left(\frac{\partial G^2}{\partial H^2} \frac{\partial G^1}{\partial \tilde{p}} - \frac{\partial G^1}{\partial H^2} \frac{\partial G^2}{\partial \tilde{p}} \right) \frac{\partial \tilde{p}}{\partial \Delta \epsilon_{\tilde{p}}}, \tag{59}$$

$$E_2 = \left(\frac{\partial G^2}{\partial H^2} \frac{\partial G^1}{\partial \Delta \epsilon_{\tilde{q}}} - \frac{\partial G^1}{\partial H^2} \frac{\partial G^2}{\partial \Delta \epsilon_{\tilde{q}}} \right) + \left(\frac{\partial G^2}{\partial H^2} \frac{\partial G^1}{\partial \tilde{q}} - \frac{\partial G^1}{\partial H^2} \frac{\partial G^2}{\partial \tilde{q}} \right) \frac{\partial \tilde{q}}{\partial \Delta \epsilon_{\tilde{q}}}, \tag{60}$$

$$E_3 = \left(-\frac{\partial G^2}{\partial H^1} \frac{\partial G^1}{\partial \Delta \epsilon_{\tilde{p}}} + \frac{\partial G^1}{\partial H^1} \frac{\partial G^2}{\partial \Delta \epsilon_{\tilde{p}}} \right) + \left(-\frac{\partial G^2}{\partial H^1} \frac{\partial G^1}{\partial \tilde{p}} + \frac{\partial G^1}{\partial H^1} \frac{\partial G^2}{\partial \tilde{p}} \right) \frac{\partial \tilde{p}}{\partial \Delta \epsilon_{\tilde{p}}}, \tag{61}$$

$$E_4 = \left(-\frac{\partial G^2}{\partial H^1} \frac{\partial G^1}{\partial \Delta \epsilon_{\tilde{q}}} + \frac{\partial G^1}{\partial H^1} \frac{\partial G^2}{\partial \Delta \epsilon_{\tilde{q}}} \right) + \left(-\frac{\partial G^2}{\partial H^1} \frac{\partial G^1}{\partial \tilde{q}} + \frac{\partial G^1}{\partial H^1} \frac{\partial G^2}{\partial \tilde{q}} \right) \frac{\partial \tilde{q}}{\partial \Delta \epsilon_{\tilde{q}}}, \tag{62}$$

where G^1 and G^2 are the functions made by regrouping the implicit function as

$$G^1 = \Delta H^1 - h^1 \left(\Delta \epsilon_{\tilde{p}}, \Delta \epsilon_{\tilde{q}}, \tilde{p}, \tilde{q}, H^1, H^2 \right), \tag{63}$$

$$G^2 = \Delta H^2 - h^2 \left(\Delta \epsilon_{\tilde{p}}, \Delta \epsilon_{\tilde{q}}, \tilde{p}, \tilde{q}, H^1, H^2 \right). \tag{64}$$

Implementing Eq. (57) into Eq. (56) leads to the reduced form of the Newton–Raphson equation:

$$\begin{bmatrix} A_{11} & A_{12} \\ A_{21} & A_{22} \end{bmatrix} \begin{bmatrix} c_{\tilde{p}} \\ c_{\tilde{q}} \end{bmatrix} = \begin{bmatrix} b_1 \\ b_2 \end{bmatrix}, \tag{65}$$

where $d\Delta \epsilon_{\tilde{p}} = c_{\tilde{p}}$ and $d\Delta \epsilon_{\tilde{q}} = c_{\tilde{q}}$, and A_{ij} and b_i are given as

$$A_{11} = \tilde{P} + \Delta \epsilon_{\tilde{p}} \left(K \frac{\partial \tilde{P}}{\partial \tilde{p}} + \frac{\partial \tilde{P}}{\partial H^1} \frac{\partial H^1}{\partial \Delta \epsilon_{\tilde{p}}} + \frac{\partial \tilde{P}}{\partial H^2} \frac{\partial H^2}{\partial \Delta \epsilon_{\tilde{p}}} \right)$$
$$+ \Delta \epsilon_{\tilde{q}} \left(K \frac{\partial \tilde{Q}}{\partial \tilde{p}} + \frac{\partial \tilde{Q}}{\partial H^1} \frac{\partial H^1}{\partial \Delta \epsilon_{\tilde{p}}} + \frac{\partial \tilde{Q}}{\partial H^2} \frac{\partial H^2}{\partial \Delta \epsilon_{\tilde{p}}} \right), \tag{66}$$

$$A_{12} = \tilde{Q} + \Delta \epsilon_{\tilde{p}} \left(-3G \frac{\partial \tilde{P}}{\partial \tilde{q}} + \frac{\partial \tilde{P}}{\partial H^1} \frac{\partial H^1}{\partial \Delta \epsilon_{\tilde{q}}} + \frac{\partial \tilde{P}}{\partial H^2} \frac{\partial H^2}{\partial \Delta \epsilon_{\tilde{q}}} \right)$$
$$+ \Delta \epsilon_{\tilde{q}} \left(-3G \frac{\partial \tilde{Q}}{\partial \tilde{q}} + \frac{\partial \tilde{Q}}{\partial H^1} \frac{\partial H^1}{\partial \Delta \epsilon_{\tilde{q}}} + \frac{\partial \tilde{Q}}{\partial H^2} \frac{\partial H^2}{\partial \Delta \epsilon_{\tilde{q}}} \right), \tag{67}$$

$$A_{21} = K \frac{\partial \phi}{\partial \tilde{p}} + \frac{\partial \phi}{\partial H^1} \frac{\partial H^1}{\partial \Delta \epsilon_{\tilde{p}}} + \frac{\partial \phi}{\partial H^2} \frac{\partial H^2}{\partial \Delta \epsilon_{\tilde{p}}}, \tag{68}$$

$$A_{22} = -3G \frac{\partial \phi}{\partial \tilde{q}} + \frac{\partial \phi}{\partial H^1} \frac{\partial H^1}{\partial \Delta \epsilon_{\tilde{q}}} + \frac{\partial \phi}{\partial H^2} \frac{\partial H^2}{\partial \Delta \epsilon_{\tilde{q}}}, \tag{69}$$

$$b_1 = -\Delta \epsilon_{\tilde{p}} \tilde{P} - \Delta \epsilon_{\tilde{q}} \tilde{Q}, \tag{70}$$

$$b_2 = -\phi. \tag{71}$$

Then the values of $\Delta \epsilon_{\tilde{p}}$ and $\Delta \epsilon_{\tilde{q}}$ are updated by

$$\Delta \epsilon_{\tilde{p}}^{n+1} = \Delta \epsilon_{\tilde{p}}^{n} + c_{\tilde{p}}, \tag{72}$$

$$\Delta \epsilon_{\tilde{q}}^{n+1} = \Delta \epsilon_{\tilde{q}}^{n} + c_{\tilde{q}} \tag{73}$$

where n is the iteration number.

Declarations

Declaration Statement All authors certify that they have no affiliations with or involvement in any organization or entity with any financial or nonfinancial interest in the subject matter or materials discussed in this manuscript.

References

Ahmad, M.I.M., Curiel-Sosa, J.L., Akbar, M., Abdullah, N.A.: Numerical inspection based on quasi-static analysis using Rousselier damage model for aluminium wingbox aircraft structure. J. Phys. Conf. Ser. **1106**, 012013 (2018)

Ahmad, M.I.M., Curiel-Sosa, J.L., Arun, S., Rongong, J.A.: An enhanced void-crack based Rousselier damage model for ductile fracture with the XFEM. Int. J. Damage Mech. **28**(6), 943–969 (2019)

Aravas, N.: On the numerical integration of a class of pressure-dependent plasticity models. Int. J. Numer. Methods Eng. **24**(7), 1395–1416 (1987)

Areias, P., Dias-da-Costa, D., Sargado, J.M., Rabczuk, T.: Element-wise algorithm for modeling ductile fracture with the Rousselier yield function. Comput. Mech. **52**(6), 1429–1443 (2013)

Arun, S.: Finite Element Modelling of Fracture and Damage in Austenitic Stainless Steel in Nuclear Power Plant. PhD Thesis, Faculty of Engineering and Physical Sciences, University of Manchester, UK (2015)

Arun, S., Sherry, A.H., Smith, M.C., Sheikh, M.: Simulations of the large-scale four point bending test using Rousselier model. Eng. Fract. Mech. **178**, 497–511 (2017)

Arun, S., Sherry, A.H., Smith, M.C., Sheikh, M.: Simulations of the large-scale four point bending test using Rousselier model. Eng. Fract. Mech. **178**, 497–511 (2017)

Azinpour, E., Cesar de Sa, J., Dos Santos, A.D.: Micromechanically-motivated phase field approach to ductile fracture. Int. J. Damage Mech. **30**(1), 46–76 (2021)

Bass, B.R., Pugh, C.E., Keeney-Walker, J., Schulz, H., Sievers, J.: CSNI Project for Fracture analyses of Large-Scale International Reference Experiments (Project FALSIRE), Division of Engineering, Office of Nuclear Regulatory Research, U.S. Nuclear Regulatory Commission Washington, pp. 1–150 (1993)

Becker, A.A., Hyde, T.H., Sun, W., Andersson, P.: Benchmarks for finite element analysis of creep continuum damage mechanics. Comput. Mater. Sci. **25**(1–2), 34–41 (2002)

Bensaada, R., Almansba, M., Ouali, M.O., Hannachi, N.E.: The Rousselier model implementation for a dynamic explicit analysis of the ductile fracture. Nat. Technol. **15**, 31 (2016)

Boyina, G.R.T., Rayavarapu, V.K., Subba Rao, V.V.: Numerical modelling and damage assessment of rotary wing aircraft cabin door using continuum damage mechanics model. Appl. Compos. Mater. **24**(1), 235–250 (2017)

Chen, L., Gong, Z., Zhao, Q.: Numerical simulation of creep crack propagation for austenitic stainless steel 0Cr18Ni9 at 550 °C. Adv. Mater. Res. **230–232**, 596–599 (2011)

Dimitri, R., Rinaldi, M., Trullo, M., Tornabene, F., Fidelibus, C.: FEM/XFEM modeling of the 3D fracturing process in transversely isotropic geomaterials. Compos. Struct. **276**, 114502 (2021)

Gaffard, V., Besson, J., Gourgues-Lorenzon, A.F.: Creep failure model of a tempered martensitic stainless steel integrating multiple deformation and damage mechanisms. Int. J. Fract. **133**(2), 139–166 (2005)

Ganjiani, M.: A thermodynamic consistent rate-dependent elastoplastic-damage model. Int. J. Damage Mech. **27**(3), 333–356 (2018)

Geng, L.Y., Gong, J.M., Liu, D., Jiang, Y.: Damage analysis and life prediction of a main steam pipeline at elevated temperature based on creep damage mechanics. In: International Conference on Sustainable Power Generation and Supply, pp. 1–6 (2009)

Gohari, S., Sharifi, S., Sharifishourabi, G., Vrcelj, Z., Abadi, R.: Effect of temperature on crack initiation in gas formed structures. J. Mech. Sci. Technol. **27**(12), 3745–3754 (2013)

Haque, M.S., Steward, G.M.: Comparative analysis of the sin-hyperbolic and Kachanov–Rabotnov creep-damage models. Int. J. Press. Vessels Piping **171**, 1–9 (2019)

Hsu, T.R., Zhai, Z.H.: A finite element algorithm for creep crack growth. Eng. Fract. Mech. **20**(3), 521–533 (1984)

Hyde, T.H., Becker, A.A., Sun, W., Williams, J.A.: Finite-element creep damage analyses of P91 pipes. Int. J. Press. Vessels Piping **83**(11–12), 853–863 (2006)

Jin, W., Arson, C.: Micromechanics based discrete damage model with multiple non-smooth yield surfaces: theoretical formulation, numerical implementation and engineering applications. Int. J. Damage Mech. **27**(5), 611–639 (2018)

Kanth, S.A., Lone, A.S., Harmain, G.A., Jameel, A.: Modeling of embedded and edge cracks in steel alloys by XFEM. Mater. Today Proc. **26**, 814–818 (2020)

Karmakov, S., Cepero-Mejías, F., Curiel-Sosa, J.L.: Numerical analysis of the delamination in CFRP laminates: VCCT and XFEM assessment. Compos. Part C, Open Access **2**, 100014 (2020)

Meng, Q., Wang, Z.: Extended finite element method for power-law creep crack growth. Eng. Fract. Mech. **127**, 148–160 (2014)

Nikbin, K.M., Smith, D.J., Webster, G.A.: Prediction of creep crack growth from uniaxial creep data. Proc. R. Soc. Lond. Ser. A, Math. Phys. Sci. **396**(1810), 183–197 (1984)

Pandey, V.B., Singh, I.V., Mishra, B.K., Ahmad, S., Rao, A.V., Kumar, V.: Creep crack simulations using continuum damage mechanics and extended finite element method. Int. J. Damage Mech. **28**(1), 3–34 (2019)

Robinson, D.N., Binienda, W.K.: Model of viscoplasticity for transversely isotropic inelastically compressible solids. J. Eng. Mech. **127**(6), 567–573 (2001)

Robinson, D.N., Pastor, M.S.: Limit pressure of a circumferentially reinforced SiCTi ring. Compos. Eng. **2**(4), 229–238 (1992)

Robinson, D.N., Binienda, W.K., Miti-Kavuma, M.: Creep and creep rupture of metallic composites. J. Eng. Mech. **118**(8), 1646–1660 (1992)

Robinson, D.N., Binienda, W.K., Ruggles, M.B.: Creep of polymer matrix composites. I: Norton/Bailey creep law for transverse isotropy. J. Eng. Mech. **129**(3), 310–317 (2003)

Rousselier, G.: Dissipation in porous metal plasticity and ductile fracture. J. Mech. Phys. Solids **49**(8), 1727–1746 (2001)

Rousselier, G., Devaux, J., Mottet, G., Devesa, G.: A methodology for ductile fracture analysis based on damage mechanics: an illustration of a local approach of fracture. In: STP27716S Nonlinear Fracture Mechanics: Volume II Elastic-Plastic Fracture, STP27716S, pp. 332–354. ASTM International, West Conshohocken, PA (1988)

Roy, N., Das, A., Ray, A.K.: Simulation and quantification of creep damage. Int. J. Damage Mech. **24**(7), 1086–1106 (2015)

Samal, M.K., Dutta, B.K., Kushwaha, H.S.: A coupled damage model for creep. Trans. Indian Inst. Met. **63**(2), 641–645 (2010)

Sanchez-Rivadeneira, A.G., Duarte, C.A., Simple, A.: First-order, well-conditioned, and optimally convergent generalized/eXtended FEM for two-and three-dimensional linear elastic fracture mechanics. Comput. Methods Appl. Mech. Eng. **372**, 113388 (2020)

Seidenfuss, M., Samal, M.K., Roos, E.: On critical assessment of the use of local and nonlocal damage models for prediction of ductile crack growth and crack path in various loading and boundary conditions. Int. J. Solids Struct. **48**(24), 3365–3381 (2011)

Serna Moreno, M.C., Curiel-Sosa, J.L., Navarro-Zafra, J., Martínez Vicente, J.L., López Cela, J.J.: Crack propagation in a chopped glass-reinforced composite under biaxial testing by means of XFEM. Compos. Struct. **119**, 264–271 (2015)

Sprave, L., Menzel, A.: A large strain gradient-enhanced ductile damage model: finite element formulation, experiment and parameter identification. Acta Mech. **231**, 5159–5192 (2020)

Tvergaard, V., Needleman, A.: Analysis of the cup-cone fracture in a round tensile bar. Acta Metall. **32**(1), 157–169 (1984)

Wang, H., Liu, Z., Xu, D., Zeng, Q., Zhuang, Z.: Extended finite element method analysis for shielding and amplification effect of a main crack interacted with a group of nearby parallel microcracks. Int. J. Damage Mech. **25**(1), 4–25 (2016)

Wen, J.F., Tu, S.T., Gao, X.L., Reddy, J.N.: Simulations of creep crack growth in 316 stainless steel using a novel creep-damage model. Eng. Fract. Mech. **98**, 169–184 (2013)

Wilkins, M.L.: Calculation of elastic-plastic flow, Lawrence Radiation Laboratory, University of California, 116(4), pp. 832–844 (1969)

Xia, L., Hyde, T.H., Becker, A.A.: An assessment of the crack tip opening displacement criterion for predicting creep crack growth. Int. J. Fract. **77**(1), 29–40 (1996)

Yatomi, M., Davies, C.M., Nikbin, K.M.: Creep crack growth simulations in 316H stainless steel. Eng. Fract. Mech. **75**(18), 5140–5150 (2008)

Zhang, Z.L.: A practical micro mechanical model based local approach methodology for the analysis of ductile fracture of welded T-joints. PhD Thesis, Lappeenranta University of Technology, Finland (1994)

Zhang, Z.L.: Explicit consistent tangent moduli with a return mapping algorithm for pressure-dependent elastoplasticity models. Comput. Methods Appl. Mech. Eng. **121**(1), 29–44 (1995a)

Zhang, Z.L.: On the accuracies of numerical integration algorithms for Gurson-based pressure-dependent elastoplastic constitutive models. Comput. Methods Appl. Mech. Eng. **121**(1), 15–28 (1995b)

Zhang, Z.L., Niemi, E.: A class of generalized mid-point algorithms for the Gurson–Tvergaard material model. Int. J. Numer. Methods Eng. **38**(12), 2033–2053 (1995)

Zhao, L., Jing, H., Han, Y., Xiu, J., Xu, L.: Prediction of creep crack growth behavior in ASME P92 steel welded joint. Comput. Mater. Sci. **61**, 185–193 (2012)